# Optimization of overlap uniformness for ptychography

**Xiaojing Huang,**[1,*] **Hanfei Yan,**[1] **Ross Harder,**[2] **Yeukuang Hwu,**[3] **Ian K. Robinson,**[4,5] **and Yong S. Chu**[1]

[1]*National Synchrotron Light Source II, Brookhaven National Laboratory, Upton, NY 11973, USA*
[2]*Advanced Photon Source, Argonne National Laboratory, Argonne, IL 60439, USA*
[3]*Institute of Physics, Academia Sinica, Taipei, 11529, Taiwan*
[4]*London Centre for Nanotechnology, University College London, London, WC1H 0AH, UK*
[5]*Research Complex at Harwell, Didcot, Oxfordshire OX11 0DE, UK*

[*]*xjhuang@bnl.gov*

**Abstract:** We demonstrate the advantages of imaging with ptychography scans that follow a Fermat spiral trajectory. This scan pattern provides a more uniform coverage and a higher overlap ratio with the same number of scan points over the same area than the presently used mesh and concentric [13] patterns. Under realistically imperfect measurement conditions, numerical simulations show that the quality of the reconstructed image is improved significantly with a Fermat spiral compared with a concentric scan pattern. The result is confirmed by the performance enhancement with experimental data, especially under low-overlap conditions. These results suggest that the Fermat spiral pattern increases the quality of the reconstructed image and tolerance to data with imperfections.



**OCIS codes:** (340.0340) X-ray optics; (100.5070) Phase retrieval; (110.3010) Image reconstruction techniques.

## References and links

1. R. Hegerl and W. Hoppe, "Dynamic theory of crystalline structure analysis by electron diffraction in inhomogeneous primary wave field," Ber. Bunsenges. Phys. Chem. **74**, 1148 (1970).
2. J. Rodenburg, A. Hurst, A. Cullis, B. Dobson, F. Pfeiffer, O. Bunk, C. David, K. Jefimovs, and I. Johnson, "Hard-X-Ray Lensless Imaging of Extended Objects," Phys. Rev. Lett. **98**, 034801 (2007).
3. P. Thibault, M. Dierolf, A. Menzel, O. Bunk, C. David, and F. Pfeiffer, "High-resolution scanning x-ray diffraction microscopy," Science **321**, 379–382 (2008).
4. M. Guizar-Sicairos and J. Fienup, "Phase retrieval with transverse translation diversity: a nonlinear optimization approach," Opt. Express **16**(10), 7264–7272 (2008).
5. A. Maiden and J. Rodenburg, "An improved ptychographical phase retrieval algorithm for diffractive imaging," Ultramicroscopy **109**, 1256–1262 (2009).
6. P. Thibault and M. Guizar-Sicairos, "Maximum-likelihood refinement for coherent diffractive imaging," New J. Phys. **14**, 063004 (2012).
7. A. Maiden, M. Humphry, M. Sarahan, B. Kraus, and J. Rodenburg, "An annealing algorithm to correct positioning errors in ptychography," Ultramicroscopy **120**, 64–72 (2012).
8. M. Beckers, T. Senkbeil, T. Gorniak, K. Giewekemeyer, T. Salditt, and A. Rosenhahn, "Drift correction in ptychographic diffractive imaging," Ultramicroscopy **126**, 44–47 (2013).
9. F. Zhang, I. Peterson, J. Vila-Comamala, A. Diaz, F. Berenguer, R. Bean, B. Chen, A. Menzel, I. Robinson, and J. Rodenburg, "Translation position determination in ptychographic coherent diffraction imaging," Opt. Express **21**(11), 13592–13606 (2013).
10. A. Tripathi, I. McNulty, and O. Shpyrko, "Ptychographic overlap constraint errors and the limits of their numerical recovery using conjugate gradient descent methods," Opt. Express **22**(2), 1452–1466 (2014).

#208693 - $15.00 USD Received 20 Mar 2014; revised 6 May 2014; accepted 7 May 2014; published 16 May 2014

11. O. Bunk, M. Dierolf, S. Kynde, I. Johnson, O. Marti, and F. Pfeiffer, "Influence of the overlap parameter on the convergence of the ptychographical iterative engine," Ultramicroscopy **108**, 481–487 (2008).
12. P. Thibault, M. Dierolf, O. Bunk, A. Menzel, and F. Pfeiffer, "Probe retrieval in ptychographic coherent diffractive imaging," Ultramicroscopy **109**, 338–343 (2009).
13. M. Dierolf, P. Thibault, A. Menzel, C. Kewish, K. Jefimovs, I. Schlichting, K. Kong, O. Bunk, and F. Pfeiffer, "Ptychographic coherent diffractive imaging of weakly scattering specimens," New J. Phys. **12**, 035017 (2010).
14. C. Kewish, P. Thibault, M. Dierolf, O. Bunk, A. Menzel, J. Vila-Comamala, K. Jefimovs, and F. Pfeiffer, "Ptychographic characterization of the wavefield in the focus of reflective hard X-ray optics," Ultramicroscopy **110**, 325–329 (2010).
15. M. Dierolf, A. Menzel, P. Thibault, P. Schneider, C. Kewish, R. Wepf, O. Bunk, and F. Pfeiffer, "Ptychographic X-ray computed tomography at the nanoscale," Nature **467**, 436–440 (2010).
16. P. Thibault and A. Menzel, "Reconstructing state mixtures from diffraction measurements," Nature **494**, 68–71 (2013).
17. X. Huang, H. Yan, E. Nazaretski, R. Conley, N. Bouet, J. Zhou, K. Lauer, L. Li, D. Eom, D. Legnini, R. Harder, I. Robinson, and Y. Chu, "11 nm hard X-ray focus from a large-aperture multilayer Laue lens," Sci. Rep. **3**, 3562 (2013).
18. H. Vogel, "A better way to construct the sunflower head," Math. Biosci. **44**, 179–189 (1979).
19. H. Huntley, *The Divine Proportion* (Dover Publications, Inc., 1970).
20. E. Lockwood, *A Book of Curves* (Cambridge University Press, 1967).
21. J. Miao, Y. Nishino, Y. Kohmura, B. Johnson, C. Song, S. Risbud, and T. Ishikawa, "Quantitative image reconstruction of GaN quantum dots from oversampled diffraction intensities alone," Phys. Rev. Lett. **95**, 085503 (2005).
22. X. Huang, H. Miao, J. Steinbrener, J. Nelson, A. Stewart, D. Shapiro, and C. Jacobsen, "Signal to noise considerations in diffraction and conventional microscopy," Opt. Express **17**(16), 13541–13553 (2009).
23. X. Huang, M. Wojcik, N. Burdet, I. Peterson, G. Morrison, D. Vine, D. Legnini, R. Harder, Y. Chu, and I. K. Robinson, "Quantitative X-ray wavefront measurements of Fresnel zone plate and K-B mirrors using phase retrieval," Opt. Express **20**(21), 24038–24048 (2012).
24. R. Wilke, M. Vassholz, and T. Salditt, "Semi-transparent central stop in high-resolution X-ray ptychography using Kirkpatrick-Baez focusing," Acta Cryst. **A69**, 490–497 (2013).
25. J. Clark, X. Huang, R. Harder and I. Robinson, "Dynamic imaging using ptychography," Phys. Rev. Lett. **112**, 113901 (2014).
26. M. Guizar-Sicairos, M. Holler, A. Diaz, J. Vila-Comamala, O. Bunk, and A. Menzel, "Role of the illumination spatial-frequency spectrum for ptychography," Phys. Rev. B **86**, 100103R (2012).
27. A. Maiden, G. Morrison, B. Kaulich, A. Gianoncelli, and J. Rodenburg, "Soft X-ray spectromicroscopy using ptychography with randomly phased illumination," Nat. Commun. **4**, 1669 (2013).
28. S. Hruszkewycz, M. Highland, M. Holt, D. Kim, C. Folkman, C. Thompson, A. Tripathi, G. Stephenson, S. Hong, and P. Fuoss, "Imaging Local Polarization in Ferroelectric Thin Films by Coherent X-Ray Bragg Projection Ptychography," Phys. Rev. Lett. **110**, 177601 (2013).
29. N. Metropolis, A. Rosenbluth, M. Rosenbluth, A. Teller, and E. Teller, "Equations of state calculations by fast computing machines," J. Chem. Phys. **21**, 1087–1092 (1953).
30. W. Press, S. Teukolsky, W. Vetterling, and B. Flannery, *Numerical Recipes in C*, 2nd ed. (Cambridge University Press, 2002).

## 1. Introduction

Ptychography, originated for electron microscopy [1], is emerging as a powerful X-ray imaging technique [2]. The method has been undergoing rapid developments to improve image quality, enhance reliability and extend its applications to a variety of new scientific problems. Ptychography relies on the information recorded in the far-field diffraction patterns when the sample is scanned through a confined coherent X-ray illumination. To provide sufficient information for a successful reconstruction, it is crucial to have adequate overlap between adjacent scan spots, so that every point of the sample is exposed multiple times, which provides a sufficiently redundant set of measurements for phase-retrieval. With *a priori* knowledge of scanning positions, the method alleviates convergence difficulties and is capable of recovering both the transmission function of the sample and the wavefront of the incident X-ray beam [3–6].

The recently development of position-correction mechanisms [4, 7–10] further relaxes the accuracy requirement on the scanning positions. Nevertheless, the choice of scan pattern layout plays a critical role in determining the performance of ptychography, because it defines

#208693 - $15.00 USD Received 20 Mar 2014; revised 6 May 2014; accepted 7 May 2014; published 16 May 2014

the real-space sampling condition: the overlap ratio and the overlap uniformness. An optimum overlap of 60% was suggested to minimize the necessary radiation dose without sacrificing the image's quality [11]. It was also pointed out that the regular periodicity in a mesh scan (as shown in Fig. 1(a)) will cause a "raster grid pathology", by introducing periodic artifacts in the reconstructed images [12]. Therefore, a scan pattern with a concentric trajectory as shown in Fig. 1(b) was proposed to eliminate translational symmetry [13], and thus remove the aforementioned artifact. The concentric scan pattern has been used widely and delivers high quality images in various applications [14–17].

Generally, an ideal scan pattern for ptychography would be expected to have two desired features: broken translational symmetry and uniform overlap. In this paper, we propose the use of the Fermat spiral pattern as an optimized scan trajectory that fulfills these two conflicting demands. The improved performance is verified through numerical simulations and experimental measurements. Our results indicate that the Fermat spiral is more robust, especially under relatively low overlap conditions.

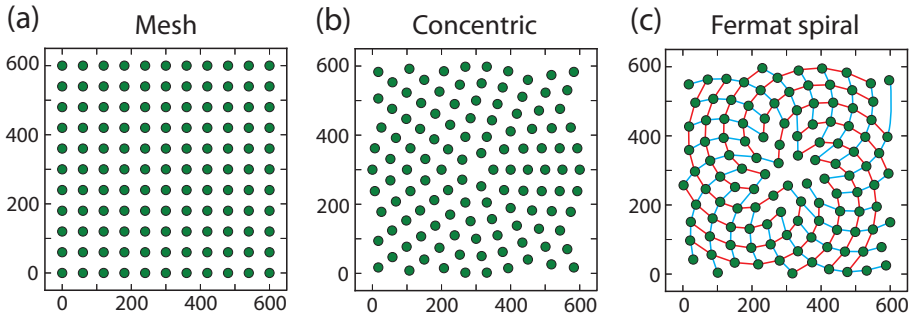


Fig. 1. Scan positions for ptychograph: (a) $11 \times 11$ mesh pattern with 121 points, (b) concentric pattern with 5 points in the first ring, 50 pixel radial increment steps and 119 points in total, (c) Fermat spiral pattern with 31 pixel increments and 119 points in total, which contains two sets of equiangular spirals: 13 clockwise (red curves) and 21 counterclockwise (blue curves). It is significant that 13 and 21 are two consecutive Fibonacci numbers.

## 2. Fermat spiral

Space optimization appears in many biological systems, such as the arrangements of the branches and leaves on the stems of plants to assure the even reception of sunlight, or the floret pattern of sunflowers for equal exposure to pollinators. Inspired by these patterns found in Nature, Vogel proposed an elegant analytic expression to construct the tight packing pattern of sunflower seeds [18]. In polar coordinates $(r, \theta)$, this has the form

$$r = c\sqrt{n}, \theta = n\phi_0, \tag{1}$$

where $c$ is a constant scaling factor for the radius, $n$ is the index number of the seed, and $\phi_0$ is the divergence angle $\sim 137.508^\circ$.

This angle $137.508^\circ$ is known as the golden angle, which divides a circle in the golden ratio $\varphi = (1+\sqrt{5})/2$, or 1.618. A rational derivation for this angle is given in [18], where the branch arrangement is optimized to be evenly spaced. Denoting the branch angular increment as $p/q$, which stands for $q$ branches making $p$ complete turns around the stem, it is shown that to ensure all branches sharing the same spatial relationship and fitting into the largest existing gap, $p$ and $q$ have to be two adjacent Fibonacci numbers of even order ($F_{2\nu}$ and $F_{2\nu+2}$). With the limitation that the number of branches goes to infinity, the optimal angular stepsize $p/q$

#208693 - $15.00 USD Received 20 Mar 2014; revised 6 May 2014; accepted 7 May 2014; published 16 May 2014

becomes $\lim_{\nu\to\infty}(F_{2\nu}/F_{2\nu+2}) = \lim_{\nu\to\infty}[(F_{2\nu}/F_{2\nu+1})(F_{2\nu+1}/F_{2\nu+2})] = 1/\varphi^2$ [19], so that the corresponding divergence angle is $\phi_0 = 2\pi/\varphi^2 \approx 137.508^\circ$.

An intuitive reason for the square-root relationship between the radius and index number arises from the requirement that each seed takes up an equal area. Assuming that $n$ seeds occupy a circular area with radius $r$, the space occupied by each seed is expected to be a constant, or $\pi r^2 \propto n$, so that the radius $r$ is proportional to $\sqrt{n}$.

Combining the equations in Eq. 1, the proposed pattern takes the form $r^2 = c^2/\phi_0 \cdot \theta$, *i.e.*, an expression for a parabolic spiral ($r^2 = \alpha\theta$), which was first discussed by P. Fermat in 1636 and named after him [20].

Figure 1(c) shows a Fermat spiral pattern that is constructed with $c = 31$ pixels and spreads over an area of 600×600 pixels. The radius scaling factor, $c$, is tuned to ensure that the total number of points matches that of the concentric pattern over the same area as illustrated in Fig.1(b). Indeed, the Fermat spiral pattern depicts the capitulum of a sunflower. The points are located at the intersections of two sets of equiangular spirals: 13 clockwise and 21 counter-clockwise, respectively, indicated as the red and blue curves in Fig. 1(c). This pattern is distributed uniformly and has neither periodicity nor noticeable symmetry, which perfectly fulfills the requirements for ptychography measurement.

## 3. Simulation result

The performance of the Fermat spiral as a scan pattern for ptychography was tested with numerical simulations. All three scan patterns shown in Fig. 1 were evaluated and compared. They cover the same $600 \times 600$ pixel area, and the total numbers of points are almost equivalent: 121, 119 and 119, respectively.

The first simulation assumes a perfect condition with no noise, no missing pixels, and no positioning inaccuracy. Figure 2(a) shows the simulated complex object and the probe used in this simulation. The ptychography reconstructions are performed with the Difference Map algorithm [3]. Each reconstruction cycle was run for 1000 iterations, with the last 200 iteration outputs averaged to give the final images. The reconstruction was repeated ten times with individual random guesses of both the object and the probe.

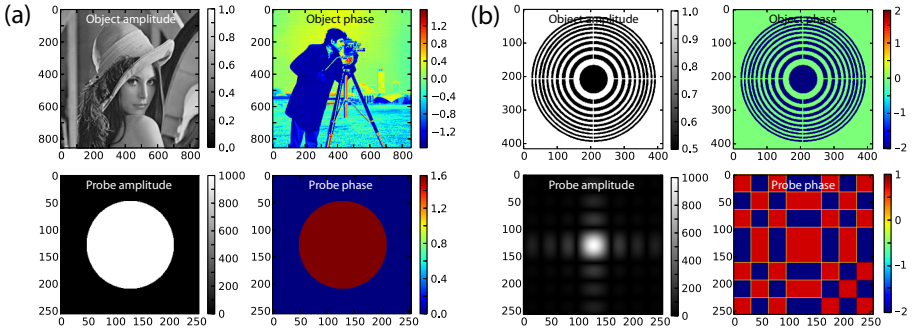


Fig. 2. Top row: Amplitudes and phases of the simulated objects. Bottom row: Amplitudes and phases of the simulated illuminations. (a) for simulation set 1, (b) for simulation set 2.

The reconstructed amplitude and phase images are shown in Fig. 3 and Fig. 4, respectively. The "raster grid pathology" clearly is evident in the reconstructed amplitude and phase images with the mesh pattern. Because the scanning points are exactly located at regular grids in this ideally controlled simulation, this pathological effect is magnified. Both the concentric and Fermat spiral scans eliminate the periodic artifact. Two criteria are used to evaluate the obtained image's quality: The real-space $R$ factor [21] that measures the difference between the original

#208693 - $15.00 USD Received 20 Mar 2014; revised 6 May 2014; accepted 7 May 2014; published 16 May 2014

image's intensity $I_0$ and the reconstructed image's intensity $I_{recon}$ as well as the signal-to-noise ratio $SNR$ estimated from the correlation coefficient $r_{cc}$ [22] that represents the similarity between reconstructed images from individual random starts. $R$ and $SNR$ are calculated as follows:

$$R = \sqrt{\frac{\langle I_0 - I_{recon} \rangle^2}{\langle I_0 + I_{recon} \rangle^2}}, \tag{2}$$

$$SNR = \sqrt{\frac{r_{cc}}{1 - r_{cc}}}, r_{cc} = \frac{\langle (I_{recon1} - \langle I_{recon1} \rangle)(I_{recon2} - \langle I_{recon2} \rangle) \rangle}{\sqrt{\langle (I_{recon1} - \langle I_{recon1} \rangle)^2 \rangle \langle (I_{recon2} - \langle I_{recon2} \rangle)^2 \rangle}}, \tag{3}$$

where $\langle\rangle$ denotes the averaged value. A higher quality image features a lower $R$ value and a higher $SNR$ value. The reconstructed phase part is evaluated using the same methods, but replacing intensity $I$ with phase $\phi$.

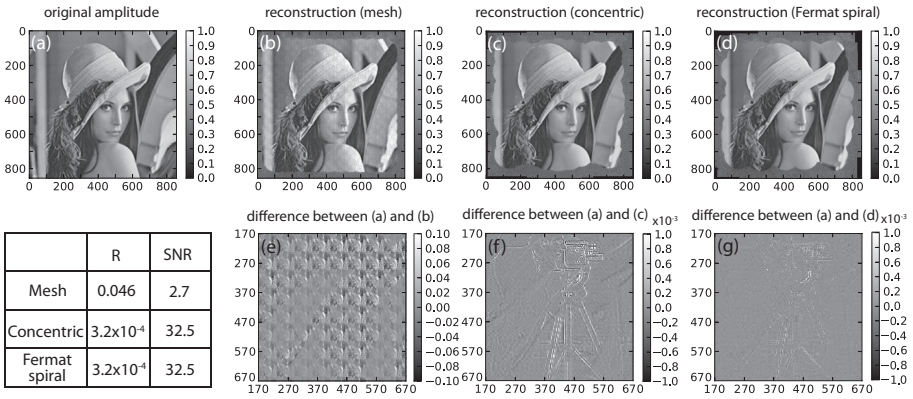


| | R | SNR |
|---|---|---|
| Mesh | 0.046 | 2.7 |
| Concentric | $3.2\times10^{-4}$ | 32.5 |
| Fermat spiral | $3.2\times10^{-4}$ | 32.5 |

Fig. 3. (a) The original object amplitude. The reconstructed amplitude using mesh pattern (b), concentric pattern (c) and Fermat spiral pattern (d). (e)(f)(g) are the difference images between the original amplitude and the reconstructed amplitudes.

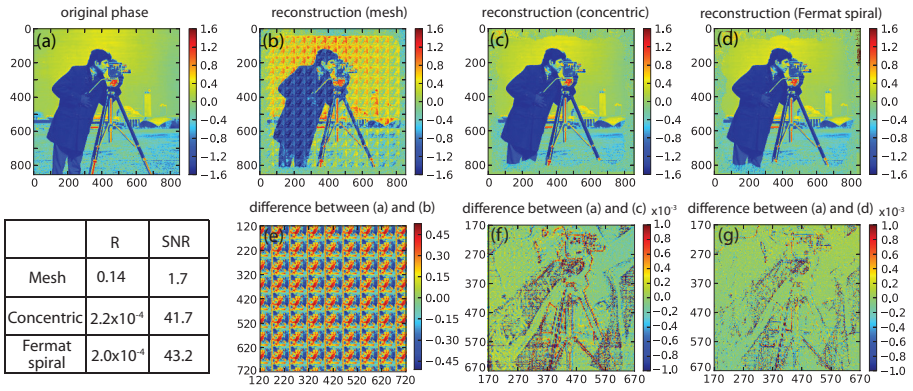


| | R | SNR |
|---|---|---|
| Mesh | 0.14 | 1.7 |
| Concentric | $2.2\times10^{-4}$ | 41.7 |
| Fermat spiral | $2.0\times10^{-4}$ | 43.2 |

Fig. 4. (a) The original object phase. The reconstructed phase using mesh pattern (b), concentric pattern (c), and Fermat spiral pattern (d). (e)(f)(g) are the difference images between the original phase and the reconstructed phases.

The central region with $500 \times 500$ pixels was used to calculate the performance criteria. For each scan pattern, 10 $R$ values and 45 $SNR$ values (there are 45 different combinations

#208693 - $15.00 USD Received 20 Mar 2014; revised 6 May 2014; accepted 7 May 2014; published 16 May 2014

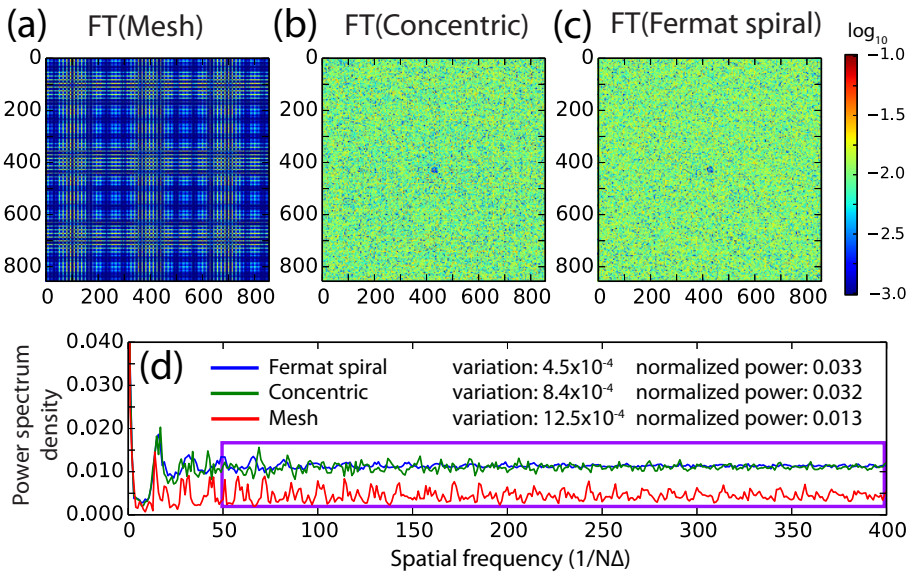


Fig. 5. (a)(b)(c): Fourier transforms of the mesh, concentric and Fermat spiral scan patterns. (d) Azimuthally averaged power spectrum density curves. Δ is denoted for the detector's pixel size. The variation and normalized power are calculated in high spatial frequency region as indicated by the purple box. The summed power is normalized by the number of points.

to select a pair out of 10 reconstructions) of both intensity and phase are estimated from 10 reconstructions. The averaged values are summarized in the inset tables of Fig. 3 and Fig. 4. For the recovered amplitude, the concentric pattern and the Fermat spiral give images of the same quality. The Fermat spiral pattern provides a slightly better phase image with improvements of 10% in *R*, and 4% in *SNR*.

To understand this slight improvement in image quality with the Fermat spiral pattern, we recall the two possible factors that can affect image quality: the overlap ratio and the overlap uniformness. These are evaluated for each tested scan pattern. The overlap ratio is estimated as

$$\sigma = \frac{\sum_{j=1}^{N-1} |P(r-r_j)||P(r-r_{j+1})|}{\sum_{j=1}^{N-1} |P(r-r_j)|^2}, \tag{4}$$

where $r_j$ stands for the translation vector for $j$th scan point. In the simulated condition, the probe has a disk shape with an 80-pixel radius, and the overlap ratios for the mesh, concentric and Fermat spiral patterns are 52.9%, 53.7% and 54.5%, respectively. The Fermat spiral only increases the overlap ratio by about 1% compared with the concentric pattern, so it is not the major contributor to the improvement of image's quality. The overlap uniformness can be studied by Fourier transforming the scan patterns (as shown in Fig. 1), and comparing the intensity and flatness of their power spectral density curve over the high spatial frequency region. As shown in Fig. 5, the Fermat spiral distributes the highest power into the high spatial frequency region. Moreover, it also gives the flattest power spectrum density curve. This is represented by the calculated standard deviation values. When calculated with spatial frequencies above 50 $1/N\Delta$ ($N$ is the number of pixels and $\Delta$ is the pixel size), the deviation values are $4.5 \times 10^{-4}$, $8.4 \times 10^{-4}$ and $12.5 \times 10^{-4}$ for the Fermat spiral, concentric and mesh scan patterns, respectively. Although these calculated deviations are subject to the selected frequency ranges, their

#208693 - $15.00 USD Received 20 Mar 2014; revised 6 May 2014; accepted 7 May 2014; published 16 May 2014

order remains the same. For instance, when calculated with frequencies above 10 ($1/N\Delta$), the frequency deviation values are $1.1\times10^{-3}$, $1.4\times10^{-3}$ and $1.6\times10^{-3}$ for Fermat spiral, concentric and mesh patterns, respectively, where the Fermat spiral still gives the lowest variation and the mesh pattern gives the largest, consistent with Fig. 5(d) calculated with frequencies above 50 ($1/N\Delta$). It implies that the Fermat spiral pattern has the potential to significantly enhance the robustness of reconstruction.

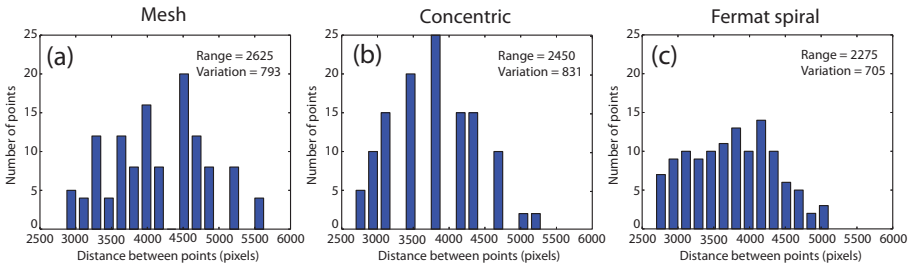


Fig. 6. Histograms of the summed distance for mesh (a), concentric (b) and Fermat spiral (c), respectively. A smaller distance distribution range and a less histogram variation indicate a more uniform overall point separation.

Another method to quantify the overlap uniformness is to estimate the separation uniformness of the scan points. For each scan point, its distances to all other points were calculated and summed. This distance summation estimates the overall separation of this specific point relative to the entire scan pattern. When the summed distance of all the scan points is plotted in a histogram, the range of distance distribution and the variation of histogram heights evaluate the separation uniformness of the scan pattern. As shown in Fig. 6, the Fermat spiral gives the most compact range of the distance distribution and lowest variation level, denoting that it provides the most uniform separation of points.

Since the ptychography reconstruction is a nonlinear process, the amount of improvement in the quality of the reconstructed image is not expected to scale exactly with the increment in overlap uniformness. With simulated perfect data, the accurately defined constraint may provide sufficient information to mitigate the influence of the overlap uniformness introduced by different scan patterns. This may explain why only about a 4% improvement in image quality was observed for the Fermat scan.

The second simulation represents a condition closer to real experimental data collection. Since both concentric and Fermat spiral capture a certain circular feature, a centro-symmetric object, as shown in Fig. 2(b), was used to encourage symmetry-introduced artifacts if they exist. An illumination function with side fringes and varying phase structure was employed to simulate a "real" probe. Only the concentric and Fermat spiral scan patterns were tested in this comparison. Poisson photon noise was added to the simulated diffraction pattern. The originally generated $256\times256$ pixel data frame was cropped to $128\times128$ pixels to mimic the finite acceptance angle of a detector in a real experiment. A random positioning error was generated with a Gaussian distribution with a 5-pixel width and assigned to each scan position. The same reconstruction process was used as in the previous simulation, with two exceptions: a noise threshold of 4 photon counts is enforced, which means that pixels with less than 4 counts were not used in the reconstruction; and an annealing-type positioning correction method [7] was used to automatically compensate for positioning errors.

Typical reconstruction results are shown in Fig. 7. Due to data cropping, the dimensions of the reconstructed object is half that of the originally simulated size in pixels, as shown in Fig. 2(b). The Fermat spiral gives a noticeably better-quality image. The quality of the recon-

#208693 - $15.00 USD Received 20 Mar 2014; revised 6 May 2014; accepted 7 May 2014; published 16 May 2014

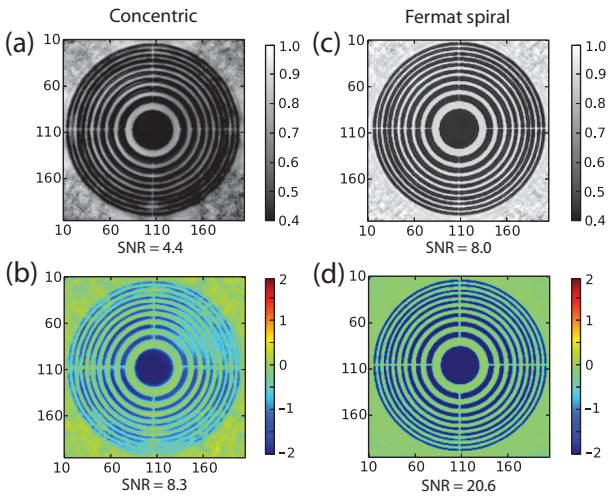


Fig. 7. Reconstruction results with noisy data and positioning error: (a) and (b) are a typical reconstructed objects' amplitude and phase with concentric scan pattern, (c) and (d) are typical reconstructions with a Fermat scan pattern.

structed images from different random starts is found to vary dramatically with the concentric scan pattern, while the Fermat spiral pattern gives consistently good reconstructions. The overall performance is evaluated using the averaged *SNR* values that show significant improvement with the Fermat spiral scan pattern, *i.e.*, 82% in amplitude and 148% in phase.

## 4. Experimental results

We compared the performances of concentric and Fermat spiral patterns with real experimental X-ray data. The measurements were conducted at Beamline 34-ID-C, at the Advanced Photon Source of Argonne National Laboratory. The instrumental setup was similar to that in a previously reported experiment [23]. Coherent 9.6 keV X-rays were focused by K-B mirrors down to about 1 $\mu$m. A star pattern made of 1.2 $\mu$m thick gold was placed near the focal plane. The sample pattern was motorized by nPoint piezo scanner NPXY100Z25. A Timepix detector with 55 $\mu$m pixel size recorded the far-field diffraction patterns, 2 meters away from the test pattern. To increase the detector's dynamic range, a $1.5 \times 1.5$ mm silicon square of 200 $\mu$m thickness was used to attenuate about 80% of the central part ($\sim 27 \times 27$ pixels) of the diffraction pattern [24, 25]. Each scan position accumulated 15 exposures with 1 second illumination time. A data array of $224 \times 224$ pixels was cropped out for reconstruction that determines the real-space pixel size of 21 nm.

Ptychography scans were collected under two overlap conditions. For the concentric pattern, the high overlap measurement scans over a $4 \times 4$ $\mu$m area with radial incremental steps of 200 nm. The less overlapped scan covers a $12 \times 12$ $\mu$m area with a 600 nm radial incremental steps. The overlap ratios are 86% and 54%, respectively. For the Fermat spiral pattern, the scanning areas cover the same ranges, with chosen scaling constants of 126 nm and 377 nm, giving the same number of measurement points as in the corresponding concentric scans. The corresponding overlap ratios are 90% and 59%, respectively. All scans consisted of 323 positions.

The same reconstruction approach with position correction and a noise threshold of 4 counts (as used in the second simulation above) was employed to recover images from the experimental data. The resulting probe intensities and object phases are shown in Fig. 8. Since the accurate complex transmission function for this gold test pattern is unknown, the *R* factor is

#208693 - $15.00 USD Received 20 Mar 2014; revised 6 May 2014; accepted 7 May 2014; published 16 May 2014

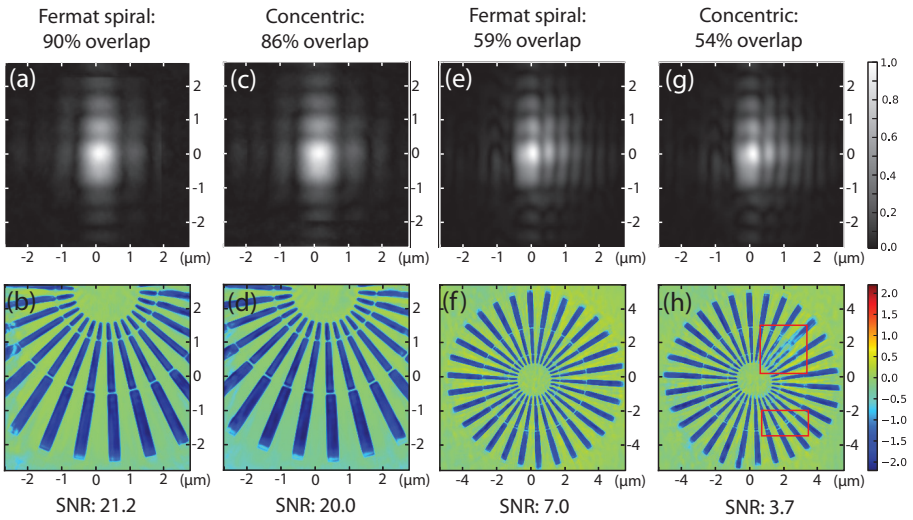


Fig. 8. Reconstructed probe amplitude (a) and object phase (b) from experimental data with Fermat spiral scan pattern at a high overlap condition. Reconstructed probe amplitude (c) and object phase (d) from experimental data with a concentric scan pattern at a high overlap condition. Reconstructed probe amplitude (e) and object phase (f) from experimental data with a Fermat spiral scan pattern at a low overlap condition. Reconstructed probe amplitude (g) and object phase (h) from experimental data with a concentric scan pattern at a low overlap condition.

difficult to calculate. The advantage of estimating *SNR* from the correlation coefficient is that information about the original image is not required. Any pair of the 10 reconstructions with different random starts can be used to estimate a *SNR* value. The obtained 45 values are then averaged. Figure 8(b) and (d) indicate that both concentric and Fermat spiral scan patterns give high quality images for high overlap ratios. The *SNR* for the Fermat spiral reconstruction is about 6% higher than that for the mesh pattern. For the less overlapped condition with the concentric pattern (shown in Fig. 8(f) and (h)), noticeable artifacts start to show in the reconstructed image, indicated by red boxes in Fig. 8(h), while the Fermat spiral pattern is able to reconstruct an image with much better quality, with about 89% improvement of *SNR*. This result confirms the conclusion of the second simulation, and implies that the Fermat spiral scan pattern offers higher tolerance to data noise and other measurement imperfections, especially in the low overlap situation.

## 5. Discussion

Broadening the spatial-frequency spectrum of the illumination probe has been proven to enhance both the fidelity and resolution of ptychography [26, 27]. This is expected to benefit measurements from weakly scattering specimens. In this study, we demonstrated that enriching and flattening the spatial-frequency spectrum of the scan pattern also improves the quality of the reconstruction image. The Fermat spiral pattern is capable to provide a robust reconstruction in relatively low overlap conditions, which can effectively reduce the required radiation dose and can be potentially beneficial for imaging biological samples. We note that a similar scan pattern previously was used in Bragg projection ptychography [28].

For optimizing the overlap ratio, another possible candidate is a hexagonal lattice structure, which is a two-dimensional close packed pattern. Adding a random noise from the regular grid

#208693 - $15.00 USD Received 20 Mar 2014; revised 6 May 2014; accepted 7 May 2014; published 16 May 2014

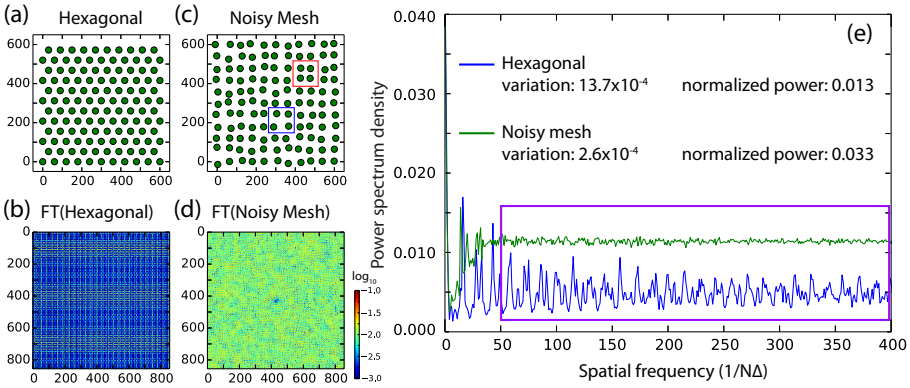


Fig. 9. (a)(b): Hexagonal scan pattern and its Fourier transform. (c)(d): Mesh scan pattern disturbed by a random positioning noise and its Fourier transform. (e) Power spectrum density curves of (c) and (d), where the variation and normalized power are calculated in the area indicated by the purple box. Deviations in local overlap are present in the noisy mesh scan pattern as shown in (c), where the overlap ratio is high in the area indicated by the red box and low in the area enclosed by the blue box.

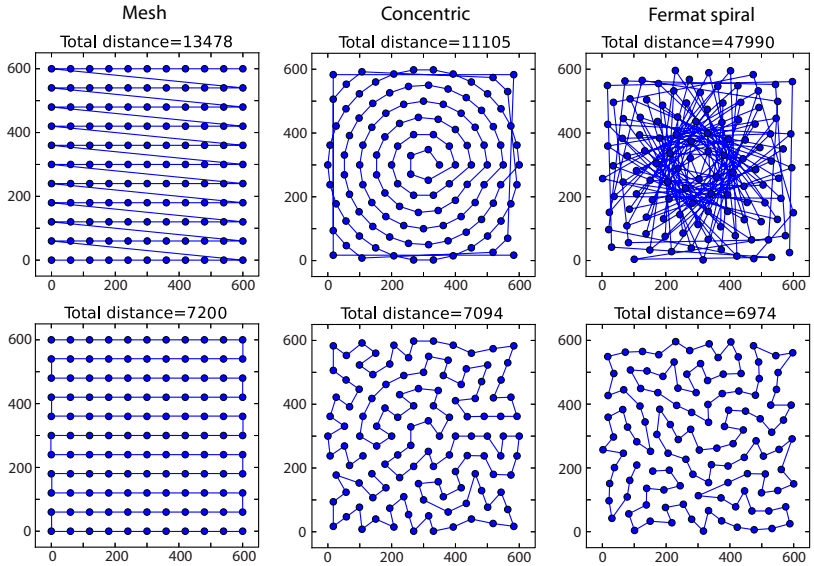


Fig. 10. Top row: The default scan trajectories for mesh, concentric and Fermat spiral patterns. Bottom row: The scan trajectories sorted by minimizing the total movement distances using the Metropolis algorithm.

#208693 - $15.00 USD Received 20 Mar 2014; revised 6 May 2014; accepted 7 May 2014; published 16 May 2014

also was been proposed to illuminate the "raster grid pathology" by removing the periodicity. Figure 9 shows two scan patterns and their power spectral density curves. In terms of the overlap uniformness, the hexagonal pattern is even slightly worse than the mesh pattern. Although the noisy mesh pattern gives a very flat azimuthally averaged power spectrum density curve, significant local variance in overlap (indicated by the red and blue boxes in Fig. 9(c)) may introduce differences in image quality from one place to another.

The Fermat spiral pattern defined by Eq. 1 naturally grows in an order from the center to edges in the same manner as the concentric pattern, as shown in the top row of Fig. 10. This allows rapid reconstructions using continuous subsets of the full ptychography dataset to visualize the central part of the object, which is the most interesting region in most cases. However, because two adjacent points in the Fermat spiral pattern are separated by $137.508^\circ$, this significantly increases the distance for motor motion. Fortunately, since high positioning accuracy is preferred, most ptychography measurements are conducted with modern piezo scanners, where the movement is completed very quickly. For other cases, if the motor's motion time is non-negligible and proportional to the moving distance, the scan trajectory can be optimized to minimize the total distance of movement. The bottom row of Fig. 10 shows the scan trajectories sorted using the Metropolis algorithm [29, 30]. The sorted Fermat spiral actually gives the shortest total travel distance.

## 6. Conclusion

The Fermat spiral defines a uniformly distributed pattern with a low symmetry that fulfills the requirements for an ideal ptychography scan trajectory. Numerical simulation shows that using Fermat spiral as a ptychography scan pattern increases image quality significantly under conditions with noise and other imperfections in measurement, compared with the concentric pattern. The improvement in performance is probably associated with increased overlap uniformness. Our conclusion is confirmed with a significant performance enhancement observed from experimental data, especially under low overlap conditions.

## Acknowledgments

Work at Brookhaven was supported by the Department of Energy, Office of Basic Energy Sciences under contract DE-AC-02-98CH10886. I.K.R. is supported by the European Resarch Council "nanosculpture" advanced grant 227711 and additional support from EPSRC. Work performed at Academia Sinica was supported by the Thematic Project (Academia Sinica), National Program for Nanoscience and Nanotechnology (the National Science Council, Taiwan). The measurements were carried out at APS beamline 34-ID-C, built with US National Science Foundation grant DMR-9724294 and operated by the US Department of Energy, Office of Basic Energy Sciences, under contract no. DE-AC-02-06CH11357.

#208693 - $15.00 USD Received 20 Mar 2014; revised 6 May 2014; accepted 7 May 2014; published 16 May 2014